OXFORD

Human Molecular Genetics, 2024, Vol. 33, 3, 233–244
https://doi.org/10.1093/hmg/ddad183
Advance access publication date 26 October 2023
Original Article

Morphological and functional alterations of neuromuscular synapses in a mouse model of *ACTA1* congenital myopathy

Yun Liu and Weichun Lin*

Department of Neuroscience, University of Texas Southwestern Medical Center, 6000 Harry Hines Blvd, Dallas, TX 75390-9111, United States
*Corresponding author. Department of Neuroscience, University of Texas Southwestern Medical Center, 6000 Harry Hines Blvd, Dallas, TX 75390-9111, United States. E-mail: weichun.lin@utsouthwestern.edu

Abstract

Mutations in skeletal muscle α-actin (Acta1) cause myopathies. In a mouse model of congenital myopathy, heterozygous Acta1 (H40Y) knock-in (*Acta1*$^{+/Ki}$) mice exhibit features of human nemaline myopathy, including premature lethality, severe muscle weakness, reduced mobility, and the presence of nemaline rods in muscle fibers. In this study, we investigated the impact of Acta1 (H40Y) mutation on the neuromuscular junction (NMJ). We found that the NMJs were markedly fragmented in *Acta1*$^{+/Ki}$ mice. Electrophysiological analysis revealed a decrease in amplitude but increase in frequency of miniature end-plate potential (mEPP) at the NMJs in *Acta1*$^{+/Ki}$ mice, compared with those in wild type (*Acta1*$^{+/+}$) mice. Evoked end-plate potential (EPP) remained similar at the NMJs in *Acta1*$^{+/Ki}$ and *Acta1*$^{+/+}$ mice, but quantal content was increased at the NMJs in *Acta1*$^{+/Ki}$, compared with *Acta1*$^{+/+}$ mice, suggesting a homeostatic compensation at the NMJs in *Acta1*$^{+/Ki}$ mice to maintain normal levels of neurotransmitter release. Furthermore, short-term synaptic plasticity of the NMJs was compromised in *Acta1*$^{+/Ki}$ mice. Together, these results demonstrate that skeletal Acta1 H40Y mutation, albeit muscle-origin, leads to both morphological and functional defects at the NMJ.

Keywords: neuromuscular junction; skeletal muscle α-actin; acetylcholine receptor; nemaline myopathy; synapse

Introduction

Skeletal muscle α-actin, the principle component of the thin filaments in adult skeletal muscle, is one of the six isoforms in the family of mammalian actin, including four muscle actins [($\alpha_{skeletal}$-actin (Acta1), $\alpha_{cardiac}$-actin (Actc1), α_{smooth}-actin (Acta2), and γ_{smooth}-actin (Actg2)] and two non-muscle actins [β_{cyto}-actin (Actb) and γ_{cyto}-actin (Actg1)] [1, 2]. Skeletal muscle α-actin plays a key role in muscle contraction by interacting with myosin in thick filaments. Mutations in skeletal muscle α-actin lead to dire consequence on muscle function. For example, muscle force production is significantly reduced in mutant mice lacking skeletal α-actin (*Acta1*$^{-/-}$), and *Acta1*$^{-/-}$ mice die during early neonatal period [3]. Clinically, mutations in the skeletal *Acta1* gene are associated with a variety of congenital myopathies. These include nemaline myopathy, intra-nuclear rod myopathy, actin-accumulation myopathy, central core disease and congenital fiber type disproportion [4–11]. The human missense mutation H40Y, located in the DNase I-binding loop of the actin sub-domain 2, greatly disrupts the binding of actin filaments to myosin molecules and therefore leads to contractile dysfunction and severe muscle weakness [12]. Human patients with the dominant *ACTA1* (H40Y) mutation develop severe muscle weakness and nemaline myopathies [4]. In a mouse model of ACTA1 nemaline myopathy, mice heterozygous for the *Acta1* (H40Y) knock-in mutation (*Acta1*$^{+/Ki}$) exhibit clinical pathology of patients with this mutation, including premature lethality, severe muscle weakness, reduced mobility, the presence of nemaline rods, and muscle fiber atrophy [13].

In this study, we sought to assess the impact of *Acta1* mutation (H40Y) on the structure and function of the NMJ. Previous studies have shown that *Acta1* mutation (H40Y) leads to marked muscle pathology in *Acta1*$^{+/Ki}$ mutant mice [13, 14], and that muscle pathology impairs the NMJs during aging [15–18] and muscular disorders such as Duchenne muscular dystrophy (DMD) [19–21]. Characterizing the effect of a muscle specific mutation such as *Acta1* mutation (H40Y) on the nerves and the NMJs would provide insights into how changes of muscle function may retrogradely affect the nerves.

We found significant changes in the structure of the NMJs in *Acta1*$^{+/Ki}$ mice when compared with their littermate *Acta1*$^{+/+}$ mice. These alterations include increased numbers of fragmentation in endplates, nerve terminals, and subsynaptic nuclei at the NMJs. These impairments were commonly displayed among fast-twitch muscle fibers such as extensor digitorum longus (EDL), slow-twitch muscle fibers such as soleus (Sol) and a mixed fiber type such as triangularis sterni muscle (TS). However, NMJ fragmentation was affected to the greatest extent in EDL, compared to Sol or TS muscles. The overall levels of expression of AChR subunit genes, especially the gamma-subunit, were also markedly increased. Furthermore, neuromuscular synaptic transmission was also markedly altered in *Acta1*$^{+/Ki}$ mutant mice. The size of spontaneous synaptic transmission, as measured by mEPP amplitude, was reduced, while the mEPP frequency was increased. EPPs remained similar, but quantal content was increased in *Acta1*$^{+/Ki}$, compared with *Acta1*$^{+/+}$ mice. In addition, synaptic plasticity was compromised in *Acta1*$^{+/Ki}$ mutant mice, indicated by a reduction in pair-pulse facilitation and an increase in synaptic depression in

Received: May 11, 2023. **Revised:** October 9, 2023. **Accepted:** October 20, 2023

Table 1. Morphometric analyses of the NMJs in *Acta1*$^{+/+}$ and *Acta1*$^{+/ki}$ mice.

Muscle	Variable	*Acta1*$^{+/+}$	*Acta1*$^{+/ki}$	P
Sol	Percentage of fragmented NMJ (%)	0	2.81 ± 1.28	0.044
	Fragment number per endplate	1.07 ± 0.25	1.02 ± 0.21	0.8648
	Endplate area (μm^2)	320.35 ± 16.88	324.45 ± 11.68	0.8253
	Dispersion index	1.57 ± 0.05	1.65 ± 0.04	0.1367
	Percentage of NMJ with faint or loss of AChR (%)	4.78 ± 0.58	16.71 ± 3.02	0.0042
	AChE area (μm^2)	381.16 ± 81.51	312.32 ± 41.36	0.3962
	Nerve occupancy	0.73 ± 0.04	0.77 ± 0.02	0.3247
	Nerve intersection	4.56 ± 0.1	5.11 ± 0.23	0.0437
EDL	Percentage of fragmented NMJ (%)	0	74.52 ± 9	7.51×10^{-5}
	Fragment number per endplate	1.69 ± 0.2	14.4 ± 1	7.2×10^{-5}
	Endplate area (μm^2)	395.9 ± 20.02	309.24 ± 14.3	0.0066
	Dispersion index	1.62 ± 0.04	2.28 ± 0.07	0.0001
	Percentage of NMJ with faint or loss of AChR (%)	6.12 ± 1.43	52.72 ± 5.36	6.88×10^{-5}
	AChE area (μm^2)	449.09 ± 33.15	364.2 ± 16.33	0.0481
	Nerve occupancy	0.77 ± 0.02	0.67 ± 0.02	0.0036
	Nerve intersection	5.28 ± 0.12	8.03 ± 0.33	9.81×10^{-5}
TS	Percentage of fragmented NMJ (%)	0	56.28 ± 6.81	7.56×10^{-5}
	Fragment number per endplate	1.58 ± 0.16	11.09 ± 0.71	0.0004
	Endplate area (μm^2)	345.74 ± 15.51	334.47 ± 12.58	0.9162
	Dispersion index	1.81 ± 0.01	2.04 ± 0.04	0.0013
	Percentage of NMJ with faint or loss of AChR (%)	2.83 ± 2.12	53.77 ± 3.44	6.62×10^{-5}
	AChE area (μm^2)	505.34 ± 26.05	554.66 ± 19.33	0.1361
	Nerve occupancy	0.83 ± 0.02	0.69 ± 0.02	0.0013
	Nerve intersection	6.05 ± 0.19	7.57 ± 0.14	0.0003

4 pairs of *Acta1*$^{+/Ki}$ and *Acta1*$^{+/+}$ littermates, aged 2 months, were employed for morphometric analysis. The total numbers of NMJs analyzed for each muscle type were as following: *Acta1*$^{+/+}$: 274 in Sol, 249 in EDL, 295 in TS; *Acta1*$^{+/Ki}$: 311 in Sol, 273 in EDL, 305 in TS.

response to trains of nerve stimuli. Together, these results demonstrate that a mutation in skeletal muscle α-actin (*Acta1* H40Y) leads to profound changes in both the structure and function of the NMJs.

Results

Fragmentation of endplates in *Acta1*$^{+/Ki}$ mice

Previous studies have shown that *Acta1*$^{+/Ki}$ mice exhibit clinical features seen in human nemaline myopathies, including premature death, severe muscle weakness, reduced mobility, the presence of nemaline rods in skeletal muscle fibers, and muscle regeneration [13]. We sought to determine to what extent the structure and function of the NMJ in *Acta1*$^{+/Ki}$ mice are impacted. We began our studies by comparing the NMJs in *Acta1*$^{+/Ki}$ mice with those of their littermate control (*Acta1*$^{+/+}$) at 2 months of age. These analyses, carried out in three muscle groups—Sol, EDL, and TS muscles, are summarized in Table 1 and the representative images are shown in Fig. 1.

The endplates of Sol, EDL and TS muscles in *Acta1*$^{+/+}$ mice normally appeared continuous and pretzel-shaped (top row in Fig. 1A). In contrast, the endplates in EDL and TS muscles of *Acta1*$^{+/Ki}$ mice appeared fragmented (arrowheads in Fig. 1A), although the endplates in Sol muscles were only moderately affected (Fig. 1A). Quantitative analyses showed that 74.5%, 56.3% and 2.8% of endplates in EDL, TS and Sol were fragmented in *Acta1*$^{+/Ki}$ mice, respectively (Table 1, Fig. 1B). On average, we found that the fragment numbers per endplate were increased by approximately 8-fold in EDL and 7-fold in TS muscles in *Acta1*$^{+/Ki}$, compared with those in *Acta1*$^{+/+}$ mice (Table 1, Fig. 1C).

Furthermore, the sizes of endplate were significantly decreased in EDL muscles in *Acta1*$^{+/Ki}$ mice compared to those in *Acta1*$^{+/+}$ mice (Table 1, Fig. 1D). The pattern of AChR localization in the EDL and TS muscles, visualized by labeling with Texas Red conjugated α-bungarotoxin, appeared more dispersed in *Acta1*$^{+/Ki}$ mice, compared with *Acta1*$^{+/+}$ mice (Fig. 1E). Specifically, AChR staining appeared homogenous in *Acta1*$^{+/+}$ muscles (top panel in Fig. 1F), but heterogeneous in *Acta1*$^{+/Ki}$ muscles—some regions were faint or even devoid of α-bungarotoxin labeling (arrowheads in Fig. 1F). Overall, 17%–54% of the NMJs in *Acta1*$^{+/Ki}$ muscles were either faint or lacking AChR labeling, whereas only 3%–6% of the NMJs in *Acta1*$^{+/+}$ muscles showed faint AChR labeling (Table 1, Fig. 1G). These results suggest a marked loss of AChRs at the endplates in *Acta1*$^{+/Ki}$ muscles. Similarly, AChE patches were fragmented in EDL and TS muscles of *Acta1*$^{+/Ki}$ mice (Fig. 1H) and the size of AChE patches in *Acta1*$^{+/Ki}$ EDL was significantly reduced compared to the control (Table 1, Fig. 1I).

To determine if endplate fragmentation occurred prior to 2 months of age, we examined mice at earlier stages, including postnatal 14 days (P14) when NMJs undergo postnatal maturation and transform from a "plaque-like" shape to a "pretzel-like" shape [22, 23] and 1-month of age. At P14, endplates in both *Acta1*$^{+/+}$ and *Acta1*$^{+/Ki}$ mice exhibited a "pretzel-like" shape (Fig. 1J). No fragmentation was observed at this stage. However, at 1 month of age, fragmented endplates were detected in *Acta1*$^{+/Ki}$ mice (arrowheads in Fig. 1K). Together, these results suggest that the NMJs of *Acta1*$^{+/Ki}$ mice developed normally up to P14 and became fragmented as early as 1 month of age.

Presynaptic defects at the NMJs in *Acta1*$^{+/Ki}$ mice

We next examined presynaptic nerve terminals using antibodies against synaptic vesicle proteins such as anti-synaptotagmin 2 (Syt 2). Consistent with the alterations seen at postsynaptic AChRs, pre-synaptic nerve terminals in *Acta1*$^{+/Ki}$ mice appeared fragmented and exhibited a bead-like staining pattern in EDL and TS muscles (arrowheads in Fig. 2B and C), but not in Sol muscles (Fig. 2A). We quantified the ratio of nerve occupancy by dividing the area of the nerve terminal by the area occupied by AChRs.

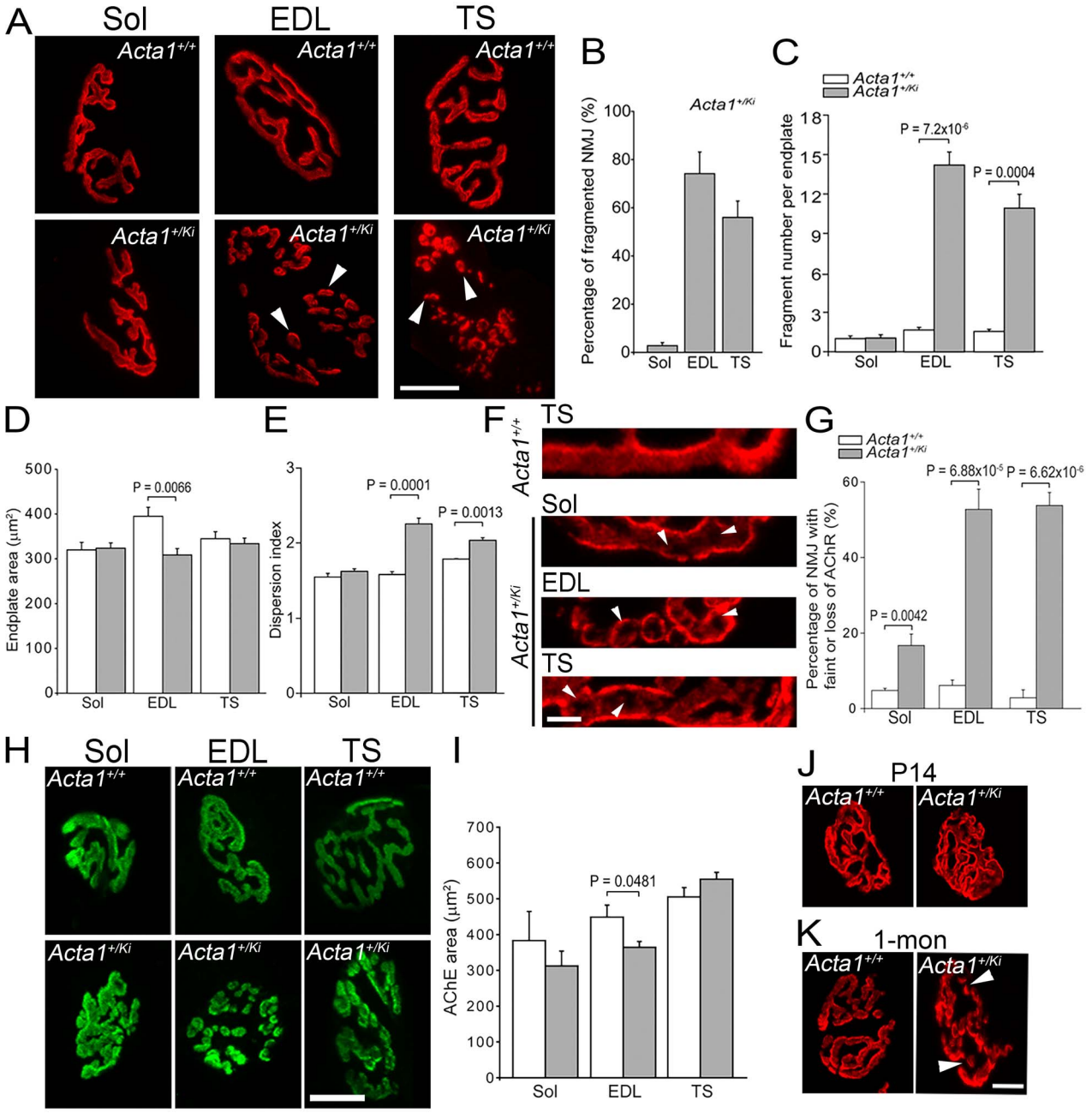

Figure 1. Fragmentation of endplates in *Acta1*$^{+/Ki}$ mice. (A–B) Whole mounts of soleus (Sol), extensor digitorum longus (EDL) and triangularis sterni (TS) muscles of *Acta1*$^{+/Ki}$ and *Acta1*$^{+/+}$ mice (2-month) were stained with α-bungarotoxin to label AChRs at the motor endplate. Note that the endplates in EDL and TS of *Acta1*$^{+/Ki}$ mice are highly fragmented (arrowheads in A), and a comparison of the percentage of fragmented endplates among Sol, EDL, and TS in *Acta1*$^{+/Ki}$ mice is shown in (B). (C) Quantification of the average fragment number per endplate between *Acta1*$^{+/+}$ and *Acta1*$^{+/Ki}$ mice. (D) Quantification of endplate size in *Acta1*$^{+/+}$ and *Acta1*$^{+/Ki}$ mice. The endplate size in EDL, but not in Sol or TS, is significantly reduced in *Acta1*$^{+/Ki}$ mice compared with that in *Acta1*$^{+/+}$ mice. (E) The dispersion index of EDL and TS, but not Sol muscles, is significantly increased in *Acta1*$^{+/Ki}$ mice compared with *Acta1*$^{+/+}$ mice. (F) High magnification views of endplates labeled with α-bungarotoxin. Note that some regions of endplates in *Acta1*$^{+/Ki}$ mice are devoid of α-bungarotoxin labeling (arrowheads). (G) Quantification of the percentages of the NMJ with faint or no AChR staining in *Acta1*$^{+/+}$ and *Acta1*$^{+/Ki}$ mice. (H and I) Whole mounts of Sol, EDL and TS muscles were labeled with antibodies against AChE. The area of AChE patches in EDL muscles is significantly decreased in *Acta1*$^{+/Ki}$ mice compared with that in *Acta1*$^{+/+}$ mice. (J and K) Endplates in TS muscles at P14 (J) and 1 month (K). Endplate fragmentation was detected at 1 month, but not 14 days (P14), of age in *Acta1*$^{+/Ki}$ mice. Scale bars: A, 20 μm; F, 5 μm; H, 20 μm; J and K, 10 μm.

The nerve occupancy ratio was comparable in Sol muscles of *Acta1*$^{+/+}$ and *Acta1*$^{+/Ki}$ mice. However, the nerve occupancy ratio in *Acta1*$^{+/Ki}$ mice was significantly reduced in EDL and TS muscles compared to in *Acta1*$^{+/+}$ mice (Table 1 and Fig. 2D). Nevertheless, presynaptic nerve terminals in *Acta1*$^{+/Ki}$ muscles were juxtaposed with the postsynaptic endplate; no denervated endplates were detected. Using anti-syntaxin1 antibodies to label pre-terminal axons, we noticed that nerve terminals appeared more complex in *Acta1*$^{+/Ki}$ mice compared to *Acta1*$^{+/+}$ mice (Fig. 2E). To quantify this phenotype, we drew a line along the longest axis across the nerve terminal and counted the number of intersections between the line and the nerve (Fig. 2E). Indeed, the number of nerve intersections was markedly increased in Sol, EDL and TS NMJs of *Acta1*$^{+/Ki}$ mice (increase by 12% in Sol, 52% in EDL and 25% in TS, respectively), compared to those of *Acta1*$^{+/+}$ mice (Table 1, Fig. 2F). Increase in nerve branching has previously been reported in aging

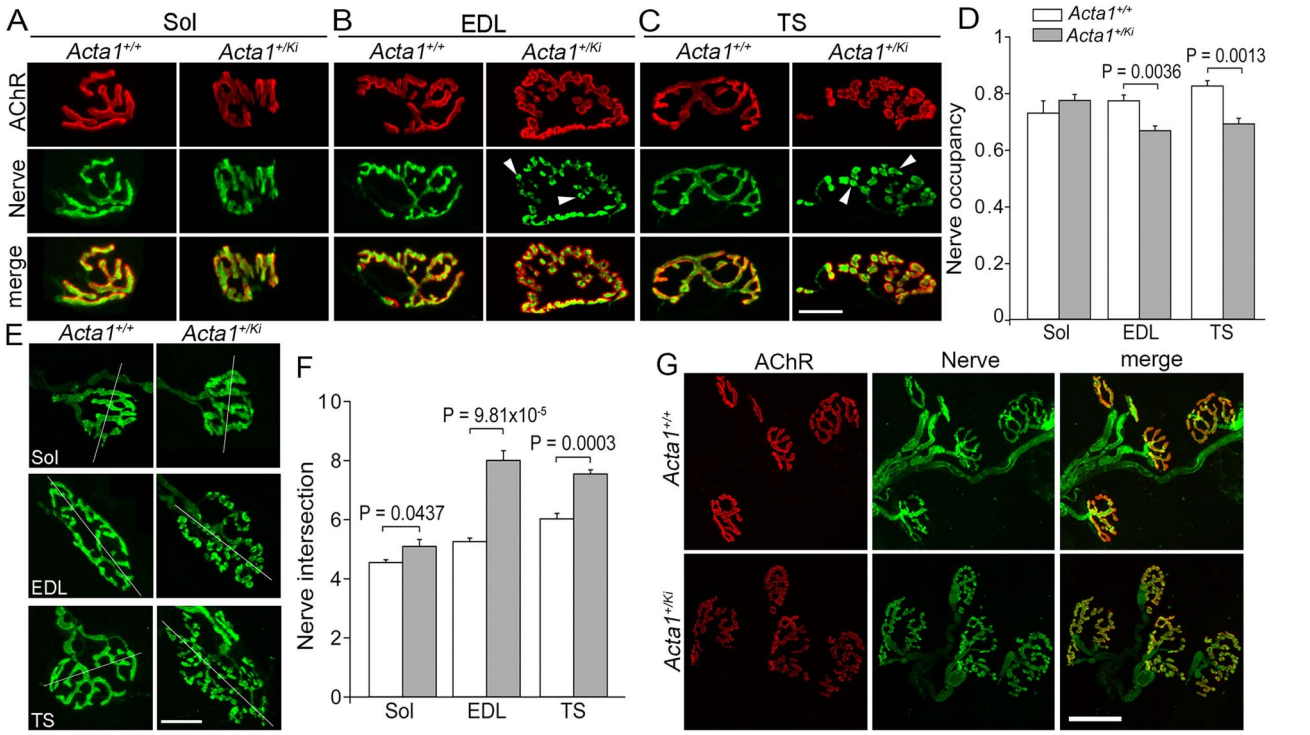

Figure 2. Pre-synaptic abnormalities *in* $Acta1^{+/Ki}$ mice. (A–C) Examples of the NMJs (2-month) revealed by double-labeling with anti-synaptotagmin 2 antibodies (nerve terminal) and α-bungarotoxin (AChR). Arrowheads point to fragmentations at the NMJs seen in EDL and TS muscles of $Acta1^{+/Ki}$ mice. (D) Quantification of nerve occupancy as a ratio of nerve terminal area over endplate area. Compared with $Acta1^{+/+}$ mice, nerve occupancy is significantly reduced at the NMJs in EDL and TS, but not Sol, of $Acta1^{+/Ki}$ mice. (E and F) Examples of pre-synaptic morphology (2-month) revealed by anti-syntaxin 1 antibody labeling, which labels both the pre-terminal nerves and the nerve terminals. To quantify the presynaptic nerves, a line was drawn along the longest axes of the terminal area and the number of intersections between the line and the nerve terminal was counted, and graphed (F). The average numbers of nerve intersection are significantly higher in $Acta1^{+/Ki}$ mice compared with $Acta1^{+/+}$ mice. (G) Examples of the NMJs in 9-month old TS muscles of $Acta1^{+/Ki}$ and $Acta1^{+/+}$ mice, revealed by double-labeling using anti-syntaxin 1 antibodies and α-bungarotoxin. Scale bars: A–C, E, G: 20 μm.

[15, 17] and dystrophic mice (such as Duchenne muscular dystrophy) [24], both of which also exhibit endplate fragmentation.

To determine if the endplate fragmentation was a precursor of denervation through die-back neuropathy that was seen in other neuromuscular disease models such as ALS, we examined NMJs in older Acta1 mutant mice (9 months of age). We observed persisting, severe NMJ fragmentation, but not denervation, in these 9-month-old $Acta1^{+/Ki}$ mice (Fig. 2G). Thus, NMJ fragmentation phenotype does not appear as a precursor of denervation in $Acta1^{+/Ki}$ mice.

Increased numbers of subsynaptic nuclei in $Acta1^{+/Ki}$ muscles

Nuclei within the synaptic region of a muscle fiber (subsynaptic nuclei) contribute to synapse-specific gene expression at the NMJ and therefore are transcriptionally distinct from those in the extra-synaptic region [25, 26]. Subsynaptic nuclei are defined as those within the synaptic region or that cross the boundary of the synaptic region [24]. Examples are shown in Fig. 3A. To distinguish myonuclei from Schwann cell nuclei, we performed triple-labeling analyses using ToPro-3, Texas Red conjugated α-bungarotoxin and S100β in whole-mount muscles (Fig. 3B and C). We counted the numbers of subsynaptic myonuclei and normalized this number to the area of the synaptic region (nuclei number per 100 μm^2 synaptic area) (Fig. 3D and E). We found that the density of subsynaptic nuclei was significantly increased in $Acta1^{+/Ki}$ mice when compared with $Acta1^{+/+}$ mice (increase by 50% in Sol, 86% in EDL, and 48% in TS respectively). These results are similar to those reported in *mdx* mice [24].

Increased levels of AChR subunit gene expression in $Acta1^{+/Ki}$ mice

To determine if the levels of gene expression were altered in $Acta1^{+/Ki}$ muscles, we performed real-time quantitative PCR to measure gene expression levels of Rapsyn, MuSK, and AChR subunits including α-, β-, δ-, ε-, and γ-subunit. We analyzed both EDL and Sol muscles from 4 pairs of $Acta1^{+/Ki}$ and their littermate $Acta1^{+/+}$ mice. As shown in Fig. 4, in both EDL and Sol muscles, the expression levels of Rapsyn and MuSK were similar between $Acta1^{+/+}$ and $Acta1^{+/Ki}$ mice. However, the expression levels of AChR subunit genes were significantly increased in $Acta1^{+/Ki}$ muscles compared with $Acta1^{+/+}$ muscles. In the EDL muscles, the expression levels of all five AChR subunits were significantly increased (Fig. 4A), and the levels of AChR γ-subunit expression were increased more than 10-folds in $Acta1^{+/Ki}$ mice compared with that in $Acta1^{+/+}$ mice. In Sol muscles, the levels of expression of AChR β and γ subunits were also significantly increased in $Acta1^{+/Ki}$ mice compared with $Acta1^{+/+}$ mice (Fig. 4B).

Altered synaptic transmission at the NMJs in $Acta1^{+/Ki}$ mice

Next, we carried out electrophysiological analysis to assess the NMJ function. We focused our analysis on EDL and Sol muscles of $Acta1^{+/Ki}$ and $Acta1^{+/+}$ mice at 2 months of age. We found that the resting membrane potentials were comparable between $Acta1^{+/+}$ and $Acta1^{+/Ki}$ muscles: $Acta1^{+/+}$ (EDL: -70.16 ± 1.73 mV, N = 4 mice, n = 46 cells; Sol: -68.91 ± 1.34 mV, N = 4, n = 47); $Acta1^{+/Ki}$ (EDL: -68.74 ± 2.1 mV, N = 4, n = 46; Sol: -68.6 ± 2.31 mV, N = 4,

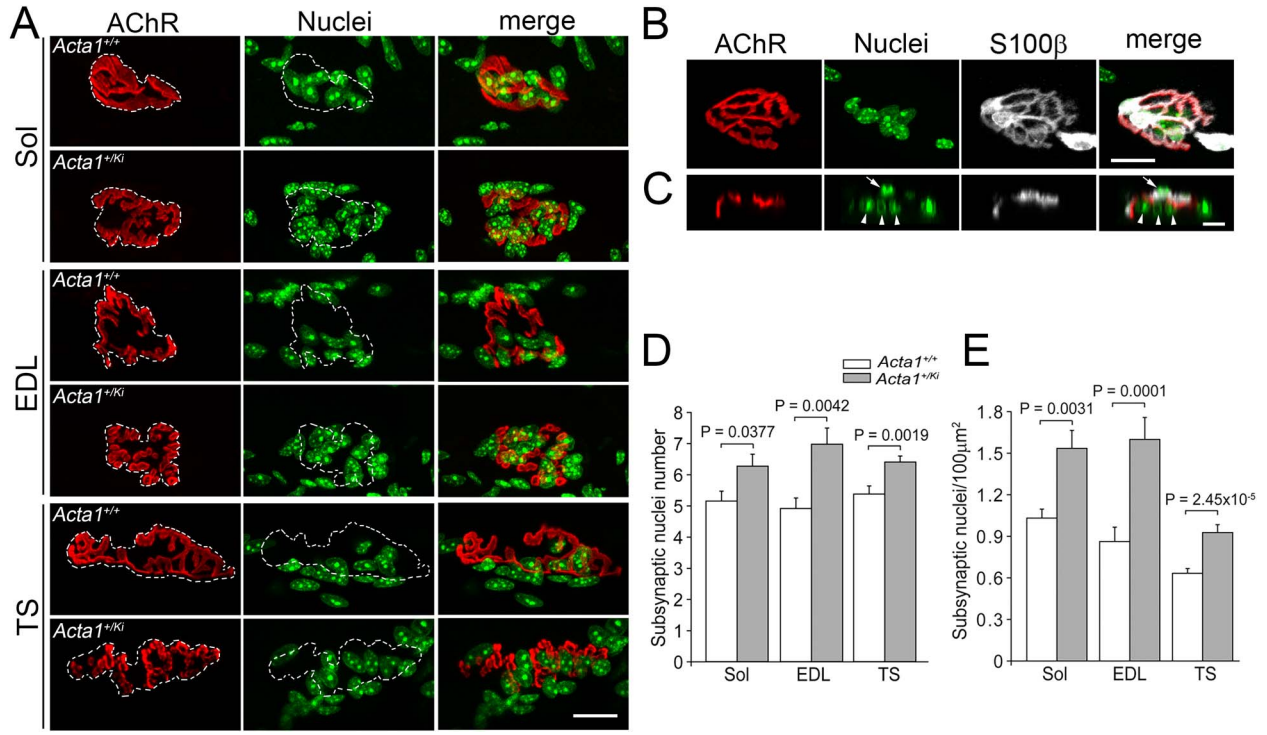

Figure 3. The number of subsynaptic nuclei is significantly increased in *Acta1*$^{+/Ki}$ mice compared with *Acta1*$^{+/+}$ mice. (A) Examples of endplate and distribution of nuclei in whole mounts of Sol, EDL and TS muscles of *Acta1*$^{+/Ki}$ and *Acta1*$^{+/+}$ mice (2-month old), double-labeled with α-bungarotoxin for AChR and ToPro-3 for nuclei. The endplate regions are highlighted by dotted lines. In both *Acta1*$^{+/+}$ and *Acta1*$^{+/Ki}$ muscles, clusters of nuclei are detected within the endplate region. (B) An example of the NMJ triple-labeled with α-bungarotoxin for AChR, ToPro-3 for nuclei and antibodies against S100β for Schwann cells. The images are maximum projection view of Z-stack sections. (C) A single section from the Z-stack in B but viewed at the Z plane by rotating the section vertically. This view plane makes it possible to distinguish subsynaptic nuclei in myofibers (arrowheads) from Schwann cells nuclei (arrow). (D) The numbers of subsynaptic nuclei are significantly increased in *Acta1*$^{+/Ki}$ mice compared with *Acta1*$^{+/+}$ mice (Sol, *Acta1*$^{+/Ki}$: 6.27 ± 0.38 *vs* *Acta1*$^{+/+}$: 5.15 ± 0.32; EDL, *Acta1*$^{+/Ki}$: 6.97 ± 0.52 *vs* *Acta1*$^{+/+}$: 4.91 ± 0.33; TS: *Acta1*$^{+/Ki}$: 6.4 ± 0.19 *vs* *Acta1*$^{+/+}$: 5.38 ± 0.26). E: Normalized number of subsynaptic nuclei to endplate region (per 100 μm^2). (Sol, *Acta1*$^{+/Ki}$: 1.54 ± 0.13 *vs* *Acta1*$^{+/+}$: 1.03 ± 0.06; EDL, *Acta1*$^{+/Ki}$: 1.6 ± 0.16 *vs* *Acta1*$^{+/+}$: 0.86 ± 0.1; TS: *Acta1*$^{+/Ki}$: 0.93 ± 0.06 *vs* *Acta1*$^{+/+}$: 0.63 ± 0.03.) scale bar in A, B: 20 μm; C: 10 μm.

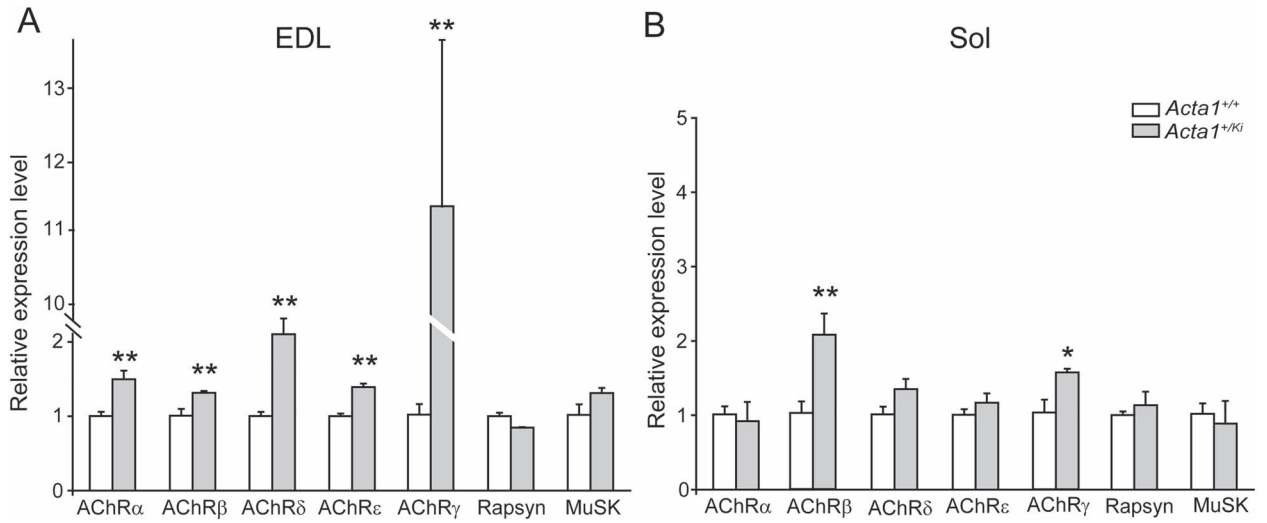

Figure 4. Elevated expression of AChR subunit genes in *Acta1*$^{+/Ki}$ mice. RT-qPCR analyses show relative expression levels of Rapsyn, MuSK and AChR α, β, δ, ε, γ subunits in EDL (A) and Sol (B) muscles of *Acta1*$^{+/Ki}$ and *Acta1*$^{+/+}$ mice (2-month old). In EDL muscles, the expression levels of all AChR subunit genes are significantly increased in *Acta1*$^{+/Ki}$ compared with *Acta1*$^{+/+}$ mice (A). Most notably, the expression of AChR γ-subunit is increased more than 10-folds in EDL muscles in *Acta1*$^{+/Ki}$ compared with that in *Acta1*$^{+/+}$ mice (A). In Sol muscles, the expression levels of AChR β and γ subunits, but not α, δ, ε subunits, are significantly increased in *Acta1*$^{+/Ki}$ mice compared with those in *Acta1*$^{+/+}$ mice. In contrast, the expression levels of Rapsyn and MuSK in both EDL and sol muscles remain similar between *Acta1*$^{+/Ki}$ and *Acta1*$^{+/+}$ muscles. *: $P < 0.05$; **: $P < 0.01$; ***: $P < 0.001$; by student *t*-test.

n = 42). However, in *Acta1*$^{+/Ki}$ mice, the frequency of spontaneous neurotransmitter release (mEPP) was increased by 48% in EDL muscles and 52% in Sol muscles, compared to *Acta1*$^{+/+}$ EDL and Sol. On the other hand, mEPP amplitudes were reduced by 22% in EDL and 18% in Sol muscles in *Acta1*$^{+/Ki}$ mice compared to those in *Acta1*$^{+/+}$ mice. No significant changes were detected in rise time

Table 2. Electrophysiological analyses of NMJs in *Acta1*$^{+/+}$ and *Acta1*$^{+/ki}$ mice.

Muscle	Variable	*Acta1*$^{+/+}$	*Acta1*$^{+/ki}$	P
EDL	MEPP frequency (Hz)	0.86 ± 0.13	1.27 ± 0.05	0.0136
	MEPP amplitude (mV)	0.96 ± 0.09	0.75 ± 0.04	0.0468
	MEPP rise time (ms)	1.22 ± 0.15	1.65 ± 0.17	0.0725
	MEPP decay time (ms)	2.42 ± 0.19	2.77 ± 0.41	0.305
Sol	MEPP frequency (Hz)	1.27 ± 0.08	1.93 ± 0.24	0.0207
	MEPP amplitude (mV)	1.11 ± 0.06	0.91 ± 0.06	0.0292
	MEPP rise time (ms)	1.43 ± 0.19	2.12 ± 0.28	0.0586
	MEPP decay time (ms)	3.49 ± 0.51	4.03 ± 0.42	0.3787
EDL	EPP amplitude (mV)	14.62 ± 1.89	17.9 ± 1.61	0.1781
	Quantal content	17.93 ± 2.63	25.47 ± 1.99	0.0282
	EPP rise time (ms)	1.1 ± 0.16	1.19 ± 0.07	0.389
	EPP decay time (ms)	6.88 ± 0.56	6.87 ± 0.72	0.6026
Sol	EPP amplitude (mV)	22 ± 0.95	24.3 ± 0.44	0.0531
	Quantal content	22.86 ± 1.33	26.71 ± 1.43	0.0355
	EPP rise time (ms)	1.24 ± 0.03	1.7 ± 0.23	0.0827
	EPP decay time (ms)	9.77 ± 0.42	11.05 ± 1.34	0.2806

4 pairs of *Acta1*$^{+/Ki}$ and *Acta1*$^{+/+}$ littermates, aged 2 months, were employed for electrophysiological analysis. The total numbers of NMJs analyzed for each muscle type were as following: *Acta1*$^{+/+}$: 46 in EDL, 46 in Sol; *Acta1*$^{+/Ki}$: 46 in EDL, 42 in Sol.

and decay time in both EDL and Sol muscles between *Acta1*$^{+/Ki}$ and *Acta1*$^{+/+}$ mice (Table 2, Fig. 5A–E).

To examine neurotransmitter release evoked by nerve action potentials, we recorded EPPs. Intriguingly, there was no significant change in EPP amplitude between *Acta1*$^{+/Ki}$ and *Acta1*$^{+/+}$ mice in both EDL and Sol muscles. However, the quantal content, which represents the quantal number of transmitter release in response to a nerve impulse, was increased by 42% in EDL and 17% in Sol in *Acta1*$^{+/Ki}$ mice, compared to those in *Acta1*$^{+/+}$ mice (Table 2 and Fig. 5F–I). Consistent with previous reports on the size of EPP [27], the amplitude of EPPs in Sol muscles was significantly larger than that of EDL muscles in both *Acta1*$^{+/+}$ and *Acta1*$^{+/Ki}$ mice.

Altered short-term synaptic plasticity in *Acta1*$^{+/Ki}$ mice

We next examined short-term facilitation by applying twin pulses at variable intervals ranging from 20–50 ms to the nerve and recorded the evoked EPPs at the NMJ (Fig. 6A). The resulting pair-pulse facilitation—a greater EPP at the second pulse [EPP(2)] compared with the first pulse [EPP(1)] has been attributed largely to the presence of residual Ca^{2+} in the nerve terminal following the first pulse [28, 29]. We found that the pair-pulse ratios [EPP(2)/EPP(1)] were significantly reduced in the NMJs of both EDL and Sol of *Acta1*$^{+/Ki}$ mice compared with those of *Acta1*$^{+/+}$ mice (Fig. 6C and D).

To further examine synaptic plasticity at the NMJs, we applied repetitive stimulation (1-s, 30 Hz) to the nerve and recorded EPPs in the muscle (Fig. 6E and F). In *Acta1*$^{+/+}$ muscles, EPPs initially exhibited moderate facilitation, and then progressed to depression before eventually reaching a plateau. EPPs recorded in *Acta1*$^{+/Ki}$ EDL and Sol muscles showed patterns like those in *Acta1*$^{+/+}$ muscles but exhibited significantly greater depression before reaching a plateau (Fig. 6G and H). These results indicate that short-term synaptic plasticity was compromised in *Acta1*$^{+/Ki}$ mice.

Discussion

In this study, we report changes at the NMJs in *Acta1*$^{+/Ki}$ mice. Previous studies have shown that these mutant mice exhibit clinical features of human congenital myopathies [4, 13], but the NMJs in these mutant mice has not been characterized. We found that *Acta1*$^{+/Ki}$ mice exhibit increased endplate fragmentation, nerve terminal complexity, subsynaptic nuclei numbers, and AChR subunit gene expression levels. Our electrophysiological analyses further show altered synaptic function at the NMJs in *Acta1*$^{+/Ki}$ mice.

As shown previously, *Acta1*$^{+/Ki}$ mice display a noteworthy disparity in premature mortality rate between male and female mice - approximately 52%–61% of mutant males die, but only 3%–5% of mutant females died by 13 weeks of age [13]. Our morphological and electrophysiological analyses reveal similar phenotype between male and female *Acta1*$^{+/Ki}$ mice (both EDL and Sol muscles) at 2 months of age (8.5 weeks). These results are consistent with the previous study by Nguyen *et al.* [13], in which they report that the reduction in twitch and titanic forces is comparable between male and female *Acta1*$^{+/Ki}$ mice at 8 weeks of age. Thus, despite differences in the rates of early lethality between male and female *Acta1*$^{+/Ki}$ mice at 13 weeks of age, both the muscle and NMJ phenotypes appear similar between male and female *Acta1*$^{+/Ki}$ mice at earlier time point (8 weeks of age).

NMJ fragmentation has been previously reported in aged and dystrophic muscle [16, 18, 19, 24, 30–32].

The mechanisms underlying NMJ fragmentation remain unclear. The NMJ undergoes remodeling and reorganization in response to muscle damage. Previous studies on the NMJs in sarcopenia and Duchenne muscular dystrophy (DMD) indicate that endplate fragmentation is likely the consequence of muscle fiber damage and degeneration [18–20, 33, 34]. Signs of focal myofiber damage (lack of eosin staining in some myofiber areas) and muscle degeneration (muscle fibers with internal nuclei) are reported in *Acta1*$^{+/Ki}$ mice [13]. Additionally, it has also been suggested that endplate fragmentation is a feature of regeneration, and therefore a process by which the efficacy of the NMJ is maintained during aging or diseases [33–37]. Our data showed that the numbers of subsynaptic nuclei are significantly increased, suggesting that regeneration and remodeling occurred at the synaptic site in *Acta1*$^{+/Ki}$ mice. Consistent with this possibility, our quantitative RT-PCR analyses showed significant increases in expression levels of AChR subunit genes in *Acta1*$^{+/Ki}$ mice.

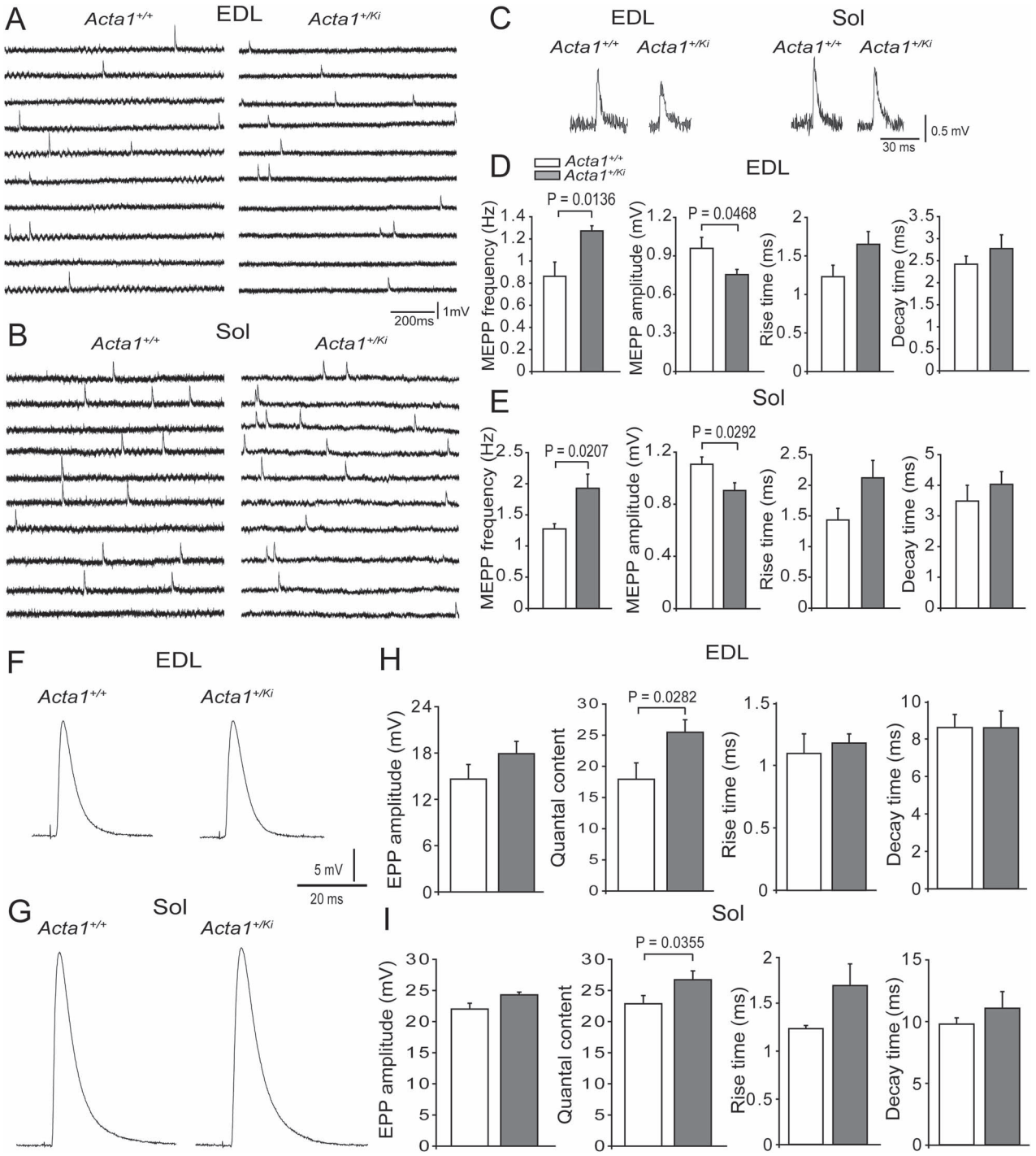

Figure 5. Alterations in transmitter release at the NMJs in *Acta1*$^{+/Ki}$ mice. (A and B) Sample traces representing a continuous recording of spontaneous activity (mEPP) for 10 s (each horizontal trace represents a 1-s recording). (C) Examples of single mEPPs at magnified scale. (D and E) Quantification of mEPP frequency, amplitude, rise time (10%~90%) and decay time (100%~50%) in EDL (D) and Sol (E). MEPP frequency is significantly increased in *Acta1*$^{+/Ki}$ mice compared with *Acta1*$^{+/+}$ mice. MEPP amplitude (normalized) is significantly reduced in *Acta1*$^{+/Ki}$ mice compared with *Acta1*$^{+/+}$ mice. (F and G) Sample EPP traces. (H and I) Quantification of EPP amplitude (corrected for non-linear summation), quantal content, rise time (10%~90%) and decay time (90%~10%). While EPP amplitudes were comparable between *Acta1*$^{+/Ki}$ and *Acta1*$^{+/+}$ mice, quantal content was significantly increased in *Acta1*$^{+/Ki}$ mice compared with that in *Acta1*$^{+/+}$ mice.

The anchoring of AChRs within the postsynaptic membrane plays crucial roles for the maturation and maintenance of the NMJ. Evidence suggests that this anchoring process is facilitated by the dystrophin-glycoprotein complex (DGC), a multicomponent structure that bridges AChR clusters between the intracellular actin cytoskeleton and the extracellular matrix [38–40]. Both human patients with Duchenne muscular dystrophy (DMD) and animal models such as mdx mice exhibit severe endplate fragmentation [18, 19, 24], similar to what we have observed in *Acta1*$^{+/Ki}$ mice. Additionally, as reported in nemaline myopathy, disorganized cortical cytoskeleton caused by mutations in α-actin may impair muscle nuclear shape, envelope and distribution [41].

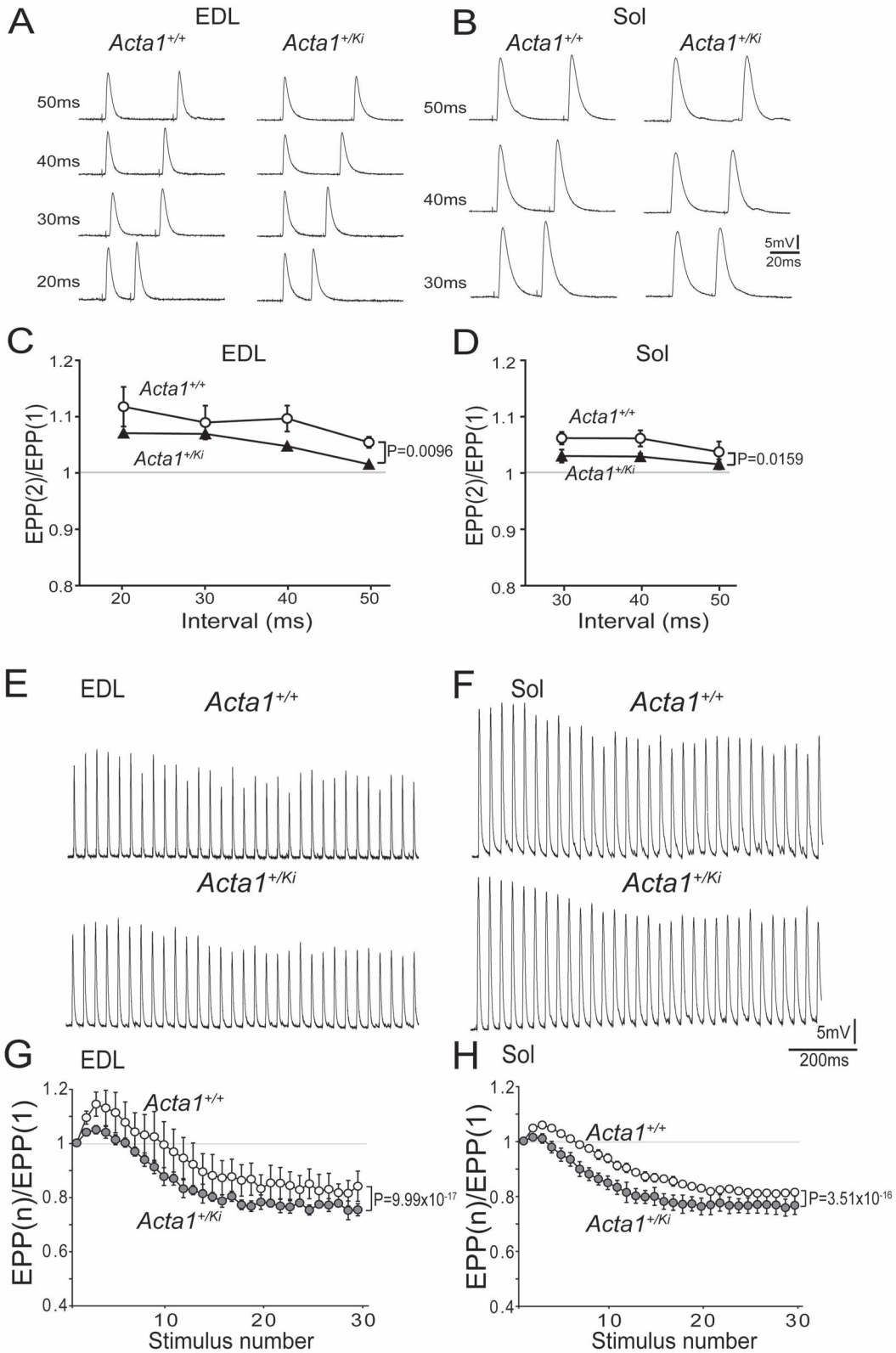

Figure 6. Impaired short-term plasticity at the NMJs in *Acta1*$^{+/Ki}$ mice. (A and B) Sample EPPs responding to pair-pulse stimulation to the nerve at various inter-pulse intervals (20–50 ms). (C and D) Quantification of pair-pulse ratio [EPP(2)/EPP(1)]. Pair-pulse facilitation is significantly decreased in both EDL and Sol in *Acta1*$^{+/Ki}$ mice compared with *Acta1*$^{+/+}$ mice. (E and F) Sample EPPs in response to a train stimulation of the nerve (1-s, 30 Hz). (G and H) Quantification of EPP run-down [EPP(n)/EPP(1)]. The ratio of EPP(n)/EPP(1) is significantly reduced in *Acta1*$^{+/Ki}$ mice compared with *Acta1*$^{+/+}$ mice.

Thus, it is plausible that altered anchorage due to disrupted cytoskeleton may contribute to endplate fragmentation and loss of AChRs in Acta1$^{+/Ki}$ mice.

In *Acta1*$^{+/Ki}$ mice, the degree of NMJ fragmentation varies among EDL, TS and Sol muscles. The difference in susceptibility to NMJ fragmentation could be due to the different extent of myopathies in different muscle fiber types in *Acta1*$^{+/Ki}$ mice. The EDL is a fast twitch muscle which is predominantly composed of Type IIb fibers, whereas the Sol is a slow twitch muscle mainly consisting of Type I and IIa fibers [42]. Indeed, a previous study has reported different muscles in *Acta1*$^{+/Ki}$ mice exhibit different extents of muscle damage [13]. While muscle fibers with internal nuclei are detected in both EDL and Sol muscles of *Acta1*$^{+/Ki}$ mice, the percentage of fibers with internal nuclei is significantly higher in EDL than that in Sol. In addition, as a common feature of nemaline myopathies, the shift towards slow fiber types (an increase in type I fiber and a concomitant decrease in type IIa fibers) is also observed in the Sol muscle of *Acta1*$^{+/Ki}$ mice [13]. Analogous muscle and fiber-type specificity in NMJ morphological alteration has been observed during aging and in neuromuscular diseases [30, 43]. For example, NMJs in EDL muscle are highly susceptible to aging; however, NMJs in extraocular muscle are strikingly resistant to damages [43]. Similarly, fast muscle fibers (type IIb) have been shown to degenerate first in Duchenne muscular dystrophy [44].

Intriguingly, mEPP frequencies are significantly increased in *Acta1*$^{+/Ki}$ mice. This suggests possible compensatory changes at affected synapses to increase presynaptic transmitter release, a homeostatic mechanism common to synapses [45, 46]. Furthermore, *Acta1*$^{+/Ki}$ mutant NMJs exhibit increased quantal content and thus normal EPP amplitude, which also indicate synaptic homeostatic modulations at *Acta1*$^{+/Ki}$ NMJs. Such mechanisms would allow synapses to enhance the release of transmitters in order to offset the reduction in AChRs and maintain the safety factor of the NMJ [46, 47]. Synaptic homeostatic compensatory mechanisms occur during aging [27, 48] as well as in neuromuscular diseases such as myasthenia gravis (MG) [49] and Duchenne muscular dystrophies [20].

In *Acta1*$^{+/Ki}$ mice, alternations at both pre-synaptic (increased release probability) and post-synaptic (increased AChR expression) at the NMJs appear insufficient to significantly improve neuromuscular function. This suggests that additional strategies are necessary to treat patients with ACTA1 myopathy. One such strategy is to target the skeletal muscle Cl- channels (CLC-1). This is based on previous elegant studies, which demonstrate that inhibition of CLC-1 via application of anthracene-9-carboxylic acid (9-AC) leads to muscle force recovery [50, 51]. Thus, it is conceivable that a similar strategy of applying 9-AC to inhibit CLC-1 may help alleviating myopathy in ACTA1 patients.

Materials and Methods

Mice

Heterozygous *Acta1* (H40Y) mutant mice (also known as 129-*Acta1*$^{tm1(H40Y;neo)Hrd}$, hereafter as *Acta1*$^{+/Ki}$) were obtained from the Jackson Laboratory at Bar Harbor, Main, USA (strain # 018284, MGI: 5424775, RRID:IMSR_JAX:018284). These mice were originally generated in the laboratory of Dr Edna Hardeman (The University of New South Wales, Sydney, Australia) [13]. The endogenous ACTA1 in these mutant mice was replaced by a mutant ACTA1 [Acta1 (H40Y) knock-in allele] carrying a single amino acid substitution of histidine to tyrosine at codon 40 (H40Y). These mice were bred with C57BL/6 J mice to generate *Acta1*$^{+/Ki}$ and littermate wild type (*Acta1*$^{+/+}$) mice for experiments.

As described previously, *Acta1*$^{+/Ki}$ mice die prematurely at 13 weeks of age [13]. Therefore, we focused our experiments on mice at 2-month of age (8.5 weeks of age, prior to premature death). Both male and female mice were included in this study. We observed no gender differences in morphological and electrophysiological analyses at the age of 2 months. Thus, the data from both sexes were combined for quantitative analyses. A total of 36 mice were analyzed, including 18 *Acta1*$^{+/Ki}$ and 18 *Acta1*$^{+/+}$ littermate mice. All experimental protocols followed National Institutes of Health Guidelines and were approved by the University of Texas Southwestern Institutional Animal Care and Use Committee.

Immunofluorescence

Whole mount immunofluorescence staining was carried out as previously described [52]. Soleus (Sol), extensor digitorum longus (EDL), and triangularis sterni (TS) muscles from *Acta1*$^{+/Ki}$ and wild type (*Acta1*$^{+/+}$) mice of postnatal 14 days (P14), 1-month, 2-month or 9-month old were fixed with 2% paraformaldehyde in 0.1 M phosphate buffer (pH 7.3) overnight at 4°C. Muscle samples were extensively washed with PBS and then incubated with Texas Red conjugated α-bungarotoxin (α-bgt) (2 nM, Invitrogen, Carlsbad, California, USA) for 30 min at room temperature. Samples were then incubated with primary antibodies overnight at 4°C. The following polyclonal antibodies were used: anti-syntaxin 1 (I375) and anti-synaptotagmin 2 (I735) (generous gifts from Dr Thomas Südhof, Stanford University School of Medicine, Palo Alto, CA, USA), anti-acetylcholinesterase (AChE) (generous gifts from Dr Palmer Taylor, Skaggs School of Pharmacy & Pharmaceutical Sciences, UC San Diego, CA, USA), and anti-S100β (Dako, Carpinteria, CA). All primary antibodies were diluted by 1:1000 in antibody dilution buffer (500 mM NaCl, 0.01 M phosphate buffer, 3% BSA, and 0.01% thimerosal). After extensive washes, muscle samples were then incubated with fluorescein isothiocyanate (FITC)-conjugated goat anti-rabbit IgG (1:600, Jackson ImmunoResearch Laboratories, Inc., West Grove, PA, USA) overnight at 4°C. For the nuclei labeling experiment, muscle samples were further incubated in ToPro-3 (1:3000, Eugene, Oregon, USA) for 30 min at room temperature. Muscle samples were mounted in the Vectashield mounting medium (H-1000, Vector Laboratories, Inc., Burlingame, CA, USA). Images were captured using a Zeiss LSM 880 confocal microscope.

Morphometric analyses

Morphometric analyses were carried using ImageJ on confocal images captured at high magnification (63× oil/N.A. 1.4). Endplate fragmentation was quantified by counting the number of discrete, fragmented AChR islands at the NMJ, based on the criteria defined by Valdez *et al.* [53] - an endplate was considered fragmented when at least 5 or more AChR islands were detected at the NMJ. The synaptic area was outlined and measured using NMJ-morph workflow similar to the procedure described in Jones *et al.* [54]. The endplate or AChE area was measured based on the area labeled by α-bungarotoxin (α-bgt) or anti-AChE antibodies, respectively. A dispersion index was obtained by dividing the synaptic area by the endplate area of the same NMJ according to the procedure described in Haddix *et al.* [34]. Presynaptic area was measured as the thresholded area labeled by anti-synaptotagmin-2 (Syt2) antibodies, which specifically labels synaptic nerve terminal but not the pre-terminal nerves. The ratio of presynaptic (nerve) area to postsynaptic (endplate) area was calculated to determine the

occupancy of presynaptic nerves at the NMJ [24]. The nerve complexity within the NMJ was determined using a procedure similar to that described by Kaplan *et al.* [55]. First, confocal images were obtained after anti-syntaxin-1 antibody staining, which labels both nerve terminals and the pre-terminal nerves. Second, a line was drawn along the longest axis across the NMJ using ImageJ. And the third, the number of intersections between the line and the axon labeled by syntaxin-1 was counted.

To quantify the numbers of subsynaptic myonuclei, whole mount muscles (EDL, Sol and TS) were triple-labeled with Texas Red conjugated α-bungarotoxin for endplates, antibodies against S100β for Schwann cells and ToPro-3 for nuclei. Subsynaptic nuclei were identified as those within the synaptic region or that cross the boundary of the synaptic region, using the criteria previously defined in Pratt *et al.* [24]. To distinguish the subsynaptic nuclei in myofibers from nuclei in Schwann cells, we adapted a procedure of optical sectioning of whole mount muscle using the procedures described previously [56, 57]. Briefly, using ImageJ analysis, z-stack sections were flipped vertically and viewed at z planes (Fig. 3C). In this angle, the location of nuclei was determined by their association with either muscle (as labeled by Texas Red conjugated α-bungarotoxin) or Schwann cells (as labeled by S100β). In this way, only the subsynaptic nuclei within the myofibers were counted; those localized in Schwann cells were excluded.

Quantitative RT-PCR

Analyses were performed using EDL and Sol muscles dissected from 4 pairs of *Acta1*$^{+/Ki}$ and *Acta1*$^{+/+}$ littermates at 2 months of age. Total RNAs were isolated by using TRI reagent (Molecular Research Center). First strand cDNAs were synthesized by using SuperScript IV VILO kit (Invitrogen). Quantitative real time PCR was carried out by using iTaq Universal SYBR Green Supermix (BIO-RAD) on a QuantStudio 6 Pro Real-Time PCR System (ThermoFisher). Housekeeping gene GAPDH was used as an internal control for quantification. The relative expression levels of the genes of interest were normalized to the levels of GAPDH of the same sample by using $\Delta\Delta$Ct method.

The following primers were used for PCR amplification: GAPDH, forward 5'-CCCACTCTTCCACCTTCGATG-3′, reverse 5'-GTCCACCACCCTGTTGCTGTAG-3′ [58]; AChR α subunit, forward 5'-CGTCTGGTGGCAAAGCT-3′, reverse 5'-CCGCTCTCCATGAAGTT-3′; AChR δ subunit, forward 5'-GTGATCTGTGTCATCGTACT-3′, reverse 5'-GCTTCTCAAACATGAGGTCA-3′; AChR ε subunit, forward 5'-AGACCTACAATGCTGAGGAGG-3′, reverse 5'-GGATGA TGAGCGTATAGATGA-3′; AChR γ subunit, forward 5'-ACGGTTGT ATCTACTGGCTG-3′, reverse 5'-GATCCA CTCAATGGCTTGC-3′ [59]. AChR β subunit, forward 5'-CAAGGCACCATGCTCAGCCTC-3′, reverse 5'-TCAGGAGCTACGAGAGGTCAT-3′ [60]. Rapsyn, forward 5'-ATATCGGGCCATGAGCCAGTAC-3′, reverse 5'-TCACAACACTCC ATGGCACTGC-3′ [61]. MuSK, forward 5'-CTCGTCCTCCCATTAAT GTAAAAA-3′, reverse 5'-TCCAGCTTCACCAGTTTGGAGTAA-3′ [59].

Electrophysiology

Neuromuscular synaptic activity was analyzed by intracellular recording on both Sol and EDL muscles isolated from 4 pairs of *Acta1*$^{+/Ki}$ and *Acta1*$^{+/+}$ littermates at 2 months of age, using procedures previously described [62]. Briefly, Sol and EDL muscles (with nerve attached) were dissected and mounted on a Sylgard coated dish, and bathed in oxygenated (95% O_2, 5% CO_2) Ringer's solution (136.8 mM NaCl, 5 mM KCl, 12 mM $NaHCO_3$, 1 mM NaH_2PO_4, 1 mM $MgCl_2$, 2 mM $CaCl_2$, and 11 mM d-glucose, pH 7.3). Endplate regions were visually identified under a water-immersion objective and impaled with glass microelectrodes (resistance 20–40 MΩ) filled with 2 M potassium citrate and 10 mM potassium chloride. Supra threshold stimuli (2–5 V, 0.1 ms) were applied to the nerve via a glass suction electrode connected to an extracellular stimulator (SD9, Grass-Telefactor, West Warwick, RI). To prevent muscle contractions, μ-conotoxin GIIIB (2 μM; Peptides International) was added to the bath solution 30 min prior to recording. Miniature endplate potentials (mEPPs) and evoked endplate potentials (EPPs) were acquired with an intracellular amplifier (AxoClamp-2B) and digitized with Digidata 1332A (Molecular Devices, Sunnyvale, CA, USA).

To calculate quantal content, EPP and mEPP amplitudes were recalibrated for non-linear summation using the methods described by Wood and Slate [63] and Roza *et al.* [64]. Data were analyzed with pClamp 10.7 (Molecular Devices) and Mini Analysis Program (Synaptosoft, Inc., Decatur, GA). The amplitudes of mEPPs and EPPs were normalized to −75 mV by using the formula $EPP_{normalized} = EPP \times (-75/V_m)$ where V_m was the measured resting membrane potential [64]. Then, the $EPP_{normalized}$ was corrected for non-linear summation by using the formula $EPP' = EPP_{normalized}/[1 - f\ (EPP_{normalized}/E)]$ [65]. The value f is a factor that improves the accuracy of non-linear summation with a consideration of the capacitance of the muscle membrane and is set to 0.8 [65, 66]. E is the difference between the resting membrane potential (V_m) and the reversal potential for ACh current, which is assumed as 0 mV [67, 68]. Next, the quantal content (the number of acetylcholine quanta released in response to a single nerve impulse) was calculated by dividing the amplitude of EPP' by the amplitude of $mEPP_{normalized}$ [63, 69]. Rise time of mEPPs or EPPs was calculated as the time for the membrane potential to rise from 10% to 90% of the peak value of mEPPs or EPPs. Decay time of mEPPs was calculated as the time for the membrane potential to decay from 100% to 50% of the peak value of mEPPs. Decay time of EPPs was calculated as the time for the membrane potential to decay from 90% to 10% of the peak value of EPPs.

Statistical analyses

Statistical analyses were performed based on the total number of mice (N) in each group, i.e. by comparing the wildtype (*Acta1*$^{+/+}$) vs the mutant (*Acta1*$^{+/Ki}$) mice. Data were presented as mean ± standard error of the mean (SEM). SigmaPlot 11.0 and Excel were used for statistical analyses. A difference with p-value of 0.05 or less would be considered statistically significant.

For quantitative morphometric analyses, statistical differences between wildtype (*Acta1*$^{+/+}$) (N = 4) and mutant (*Acta1*$^{+/Ki}$) (N = 4) were calculated using student t-test for the following parameters: the percentage of fragmented NMJs, average fragment number per endplate, endplate and AChE patch size, dispersion index of AChR, percentage of the NMJ with faint or loss of AChR stain, nerve occupancy to the endplate, nerve intersection number and subsynaptic nuclei number and density. These analyses were carried for all three muscle groups: Sol, EDL and TS muscles.

For electrophysiological data, student t-test was applied for the following parameters: mEPP frequency, amplitude, rise time (10%∼90%), decay time (100%∼50%) and EPP amplitude, quantal content, EPP rise time (10%∼90%) and decay time (90%∼10%). And student paired t-test were applied for paired-pulse and repetitive stimulation analyses. Statistical differences between wildtype (*Acta1*$^{+/+}$) (N = 4) and mutant (*Acta1*$^{+/Ki}$) (N = 4) were determined.

Conflict of interest statement: The authors declare no competing interests.

Funding

We would like to thank Ms Qiaohong Ye for her excellent technical assistant, and Drs. Joseph McArdle, Beverly Rothermel and Ben Szaro for their critical comments on earlier drafts of the manuscript. This work was supported by grants from The Paul D. Wellstone Muscular Dystrophy Cooperative Research Center (grant number: HD-087351) and the National Institutes of Health/National Institute of Neurological Disorders and Strokes (NIH/NINDS) (grant number: R01 NS055028).

Data availability

The data are available upon reasonable request.

References

1. Perrin BJ, Ervasti JM. The actin gene family: function follows isoform. *Cytoskeleton (Hoboken)* 2010;**67**:630–4.
2. Kashina AS. Regulation of actin isoforms in cellular and developmental processes. *Semin Cell Dev Biol* 2020;**102**:113–21.
3. Crawford K, Flick R, Close L. *et al.* Mice lacking skeletal muscle actin show reduced muscle strength and growth deficits and die during the neonatal period. *Mol Cell Biol* 2002;**22**:5887–96.
4. Nowak KJ, Wattanasirichaigoon D, Goebel HH. *et al.* Mutations in the skeletal muscle alpha-actin gene in patients with actin myopathy and nemaline myopathy. *Nat Genet* 1999;**23**:208–12.
5. Ilkovski B, Cooper ST, Nowak K. *et al.* Nemaline myopathy caused by mutations in the muscle alpha-skeletal-actin gene. *Am J Hum Genet* 2001;**68**:1333–43.
6. Sparrow JC, Nowak KJ, Durling HJ. *et al.* Muscle disease caused by mutations in the skeletal muscle alpha-actin gene (ACTA1). *Neuromuscul Disord* 2003;**13**:519–31.
7. Laing NG, Clarke NF, Dye DE. *et al.* Actin mutations are one cause of congenital fibre type disproportion. *Ann Neurol* 2004;**56**:689–94.
8. Wallefeld W, Krause S, Nowak KJ. *et al.* Severe nemaline myopathy caused by mutations of the stop codon of the skeletal muscle alpha actin gene (ACTA1). *Neuromuscul Disord* 2006;**16**:541–7.
9. Yang L, Yu P, Chen X. *et al.* The de novo missense mutation N117S in skeletal muscle α-actin 1 causes a mild form of congenital nemaline myopathy. *Mol Med Rep* 2016;**14**:1693–6.
10. Agrawal PB, Strickland CD, Midgett C. *et al.* Heterogeneity of nemaline myopathy cases with skeletal muscle alpha-actin gene mutations. *Ann Neurol* 2004;**56**:86–96.
11. Nowak KJ, Ravenscroft G, Laing NG. Skeletal muscle α-actin diseases (actinopathies): pathology and mechanisms. *Acta Neuropathol* 2013;**125**:19–32.
12. Chan C, Fan J, Messer AE. *et al.* Myopathy-inducing mutation H40Y in ACTA1 hampers actin filament structure and function. *Biochim Biophys Acta* 2016;**1862**:1453–8.
13. Nguyen MA, Joya JE, Kee AJ. *et al.* Hypertrophy and dietary tyrosine ameliorate the phenotypes of a mouse model of severe nemaline myopathy. *Brain* 2011;**134**:3516–29.
14. Lindqvist J, Cheng AJ, Renaud G. *et al.* Distinct underlying mechanisms of limb and respiratory muscle fiber weaknesses in nemaline myopathy. *J Neuropathol Exp Neurol* 2013;**72**:472–81.
15. Li L, Xiong WC, Mei L. Neuromuscular junction formation, aging, and disorders. *Annu Rev Physiol* 2018;**80**:159–88.
16. Gonzalez-Freire M, de Cabo R, Studenski SA. *et al.* The neuromuscular junction: aging at the crossroad between nerves and muscle. *Front Aging Neurosci* 2014;**6**:208.
17. Jang YC, Van Remmen H. Age-associated alterations of the neuromuscular junction. *Exp Gerontol* 2011;**46**:193–8.
18. Rudolf R, Khan MM, Labeit S. *et al.* Degeneration of neuromuscular junction in age and dystrophy. *Front Aging Neurosci* 2014;**6**:99.
19. Lovering RM, Iyer SR, Edwards B. *et al.* Alterations of neuromuscular junctions in Duchenne muscular dystrophy. *Neurosci Lett* 2020;**737**:135304.
20. van der Pijl EM, van Putten M, Niks EH. *et al.* Characterization of neuromuscular synapse function abnormalities in multiple Duchenne muscular dystrophy mouse models. *Eur J Neurosci* 2016;**43**:1623–35.
21. Theroux MC, Olivant A, Akins RE. C Histomorphology of neuromuscular junction in Duchenne muscular dystrophy. *Paediatr Anaesth* 2008;**18**:256–9.
22. Marques MJ, Conchello JA, Lichtman JW. From plaque to pretzel: fold formation and acetylcholine receptor loss at the developing neuromuscular junction. *J Neurosci* 2000;**20**:3663–75.
23. Sanes JR, Lichtman JW. Development of the vertebrate neuromuscular junction. *Annu Rev Neurosci* 1999;**22**:389–442.
24. Pratt SJP, Valencia AP, Le GK. *et al.* Pre- and postsynaptic changes in the neuromuscular junction in dystrophic mice. *Front Physiol* 2015;**6**:252.
25. Hippenmeyer S, Huber RM, Ladle DR. *et al.* ETS transcription factor Erm controls subsynaptic gene expression in skeletal muscles. *Neuron* 2007;**55**:726–40.
26. Schaeffer L, de Kerchove d'Exaerde A, Changeux JP. Targeting transcription to the neuromuscular synapse. *Neuron* 2001;**31**:15–22.
27. Banker BQ, Kelly SS, Robbins N. Neuromuscular transmission and correlative morphology in young and old mice. *J Physiol* 1983;**339**:355–77.
28. Jackman SL, Regehr WG. The mechanisms and functions of synaptic facilitation. *Neuron* 2017;**94**:447–64.
29. Zucker RS, Regehr WG. Short-term synaptic plasticity. *Annu Rev Physiol* 2002;**64**:355–405.
30. Prakash YS, Sieck GC. Age-related remodeling of neuromuscular junctions on type-identified diaphragm fibers. *Muscle Nerve* 1998;**21**:887–95.
31. Harris JB, Ribchester RR. The relationship between end-plate size and transmitter release in normal and dystrophic muscles of the mouse. *J Physiol* 1979;**296**:245–65.
32. Valenzuela IMY, Chen PJ, Barden J. *et al.* Distinct roles of the dystrophin-glycoprotein complex: α-dystrobrevin and α-syntrophin in the maintenance of the postsynaptic apparatus of the neuromuscular synapse. *Hum Mol Genet* 2022;**31**:2370–85.
33. Lyons PR, Slater CR. Structure and function of the neuromuscular junction in young adult mdx mice. *J Neurocytol* 1991;**20**:969–81.
34. Haddix SG, Lee YI, Kornegay JN. *et al.* Cycles of myofiber degeneration and regeneration lead to remodeling of the neuromuscular junction in two mammalian models of Duchenne muscular dystrophy. *PLoS One* 2018;**13**:e0205926.
35. Slater CR. 'Fragmentation' of NMJs: a sign of degeneration or regeneration? A long journey with many junctions. *Neuroscience* 2020;**439**:28–40.
36. Li Y, Lee Y, Thompson WJ. Changes in aging mouse neuromuscular junctions are explained by degeneration and regeneration of muscle fiber segments at the synapse. *J Neurosci* 2011;**31**:14910–9.
37. Li Y, Thompson WJ. Nerve terminal growth remodels neuromuscular synapses in mice following regeneration of the postsynaptic muscle fiber. *J Neurosci* 2011;**31**:13191–203.
38. Belhasan DC, Akaaboune M. The role of the dystrophin glycoprotein complex on the neuromuscular system. *Neurosci Lett* 2020;**722**:134833.

39. Shi L, Fu AK, Ip NY. Molecular mechanisms underlying maturation and maintenance of the vertebrate neuromuscular junction. *Trends Neurosci* 2012;**35**:441–53.
40. Banks GB, Fuhrer C, Adams ME. *et al.* The postsynaptic submembrane machinery at the neuromuscular junction: requirement for rapsyn and the utrophin/dystrophin-associated complex. *J Neurocytol* 2003;**32**:709–26.
41. Ross JA, Levy Y, Ripolone M. *et al.* Impairments in contractility and cytoskeletal organisation cause nuclear defects in nemaline myopathy. *Acta Neuropathol* 2019;**138**:477–95.
42. Schiaffino S, Reggiani C. Fiber types in mammalian skeletal muscles. *Physiol Rev* 2011;**91**:1447–531.
43. Valdez G, Tapia JC, Lichtman JW. *et al.* Shared resistance to aging and ALS in neuromuscular junctions of specific muscles. *PLoS One* 2012;**7**:e34640.
44. Webster C, Silberstein L, Hays AP. *et al.* Fast muscle fibers are preferentially affected in Duchenne muscular dystrophy. *Cell* 1988;**52**:503–13.
45. Davis GW. Homeostatic signaling and the stabilization of neural function. *Neuron* 2013;**80**:718–28.
46. Davis GW, Muller M. Homeostatic control of presynaptic neurotransmitter release. *Annu Rev Physiol* 2015;**77**:251–70.
47. Ruff RL. Endplate contributions to the safety factor for neuromuscular transmission. *Muscle Nerve* 2011;**44**:854–61.
48. Willadt S, Nash M, Slater CR. Age-related fragmentation of the motor endplate is not associated with impaired neuromuscular transmission in the mouse diaphragm. *Sci Rep* 2016;**6**:24849.
49. Plomp JJ, Morsch M, Phillips WD. *et al.* Electrophysiological analysis of neuromuscular synaptic function in myasthenia gravis patients and animal models. *Exp Neurol* 2015;**270**:41–54.
50. Pedersen TH, Macdonald WA, Broch-Lips M. *et al.* Chloride channel inhibition improves neuromuscular function under conditions mimicking neuromuscular disorders. *Acta Physiol (Oxf)* 2021;**233**:e13690.
51. Voss AA. Extracellular ATP inhibits chloride channels in mature mammalian skeletal muscle by activating P2Y1 receptors. *J Physiol* 2009;**587**:5739–52.
52. Liu Y, Padgett D, Takahashi M. *et al.* Essential roles of the acetylcholine receptor gamma-subunit in neuromuscular synaptic patterning. *Development* 2008;**135**:1957–67.
53. Valdez G, Tapia JC, Kang H. *et al.* Attenuation of age-related changes in mouse neuromuscular synapses by caloric restriction and exercise. *Proc Natl Acad Sci U S A* 2010;**107**:14863–8.
54. Jones RA, Reich CD, Dissanayake KN. *et al.* NMJ-morph reveals principal components of synaptic morphology influencing structure-function relationships at the neuromuscular junction. *Open Biol* 2016;**6**:160240. https://doi.org/10.1098/rsob.160240.
55. Kaplan MM, Sultana N, Benedetti A. *et al.* Calcium influx and release cooperatively regulate AChR patterning and motor axon outgrowth during neuromuscular junction formation. *Cell Rep* 2018;**23**:3891–904.
56. Oury J, Liu Y, Topf A. *et al.* MACF1 links Rapsyn to microtubule- and actin-binding proteins to maintain neuromuscular synapses. *J Cell Biol* 2019;**218**:1686–705.
57. Grady RM, Starr DA, Ackerman GL. *et al.* Syne proteins anchor muscle nuclei at the neuromuscular junction. *Proc Natl Acad Sci U S A* 2005;**102**:4359–64.
58. Taetzsch T, Tenga MJ, Valdez G. Muscle fibers secrete FGFBP1 to slow degeneration of neuromuscular synapses during aging and progression of ALS. *J Neurosci* 2017;**37**:70–82.
59. Tang H, Goldman D. Activity-dependent gene regulation in skeletal muscle is mediated by a histone deacetylase (HDAC)-Dach2-myogenin signal transduction cascade. *Proc Natl Acad Sci U S A* 2006;**103**:16977–82.
60. Poea-Guyon S, Christadoss P, Le Panse R. *et al.* Effects of cytokines on acetylcholine receptor expression: implications for myasthenia gravis. *J Immunol* 2005;**174**:5941–9.
61. Wang J, Ruan NJ, Qian L. *et al.* Wnt/beta-catenin signaling suppresses Rapsyn expression and inhibits acetylcholine receptor clustering at the neuromuscular junction. *J Biol Chem* 2008;**283**:21668–75.
62. Liu Y, Sugiura Y, Lin W. The role of Synaptobrevin1/VAMP1 in Ca2+−triggered neurotransmitter release at the mouse neuromuscular junction. *J Physiol* 2011;**589**:1603–18.
63. Wood SJ, Slater CR. Safety factor at the neuromuscular junction. *Prog Neurobiol* 2001;**64**:393–429.
64. Rozas JL, Gomez-Sanchez L, Tomas-Zapico C. *et al.* Increased neurotransmitter release at the neuromuscular junction in a mouse model of polyglutamine disease. *J Neurosci* 2011;**31**:1106–13.
65. McLachlan EM, Martin AR. Non-linear summation of end-plate potentials in the frog and mouse. *J Physiol* 1981;**311**:307–24.
66. Martin AR. The effect of membrane capacitance on non-linear summation of synaptic potentials. *J Theor Biol* 1976;**59**:179–87.
67. Magleby KL, Stevens CF. The effect of voltage on the time course of end-plate currents. *J Physiol* 1972;**223**:151–71.
68. Magleby KL, Stevens CF. A quantitative description of end-plate currents. *J Physiol* 1972;**223**:173–97.
69. Boyd IA, Martin AR. The end-plate potential in mammalian muscle. *J Physiol* 1956;**132**:74–91.